X-ray spectroscopy of $E2$ and $M3$ transitions in Ni-like W

J. Clementson,* P. Beiersdorfer, and M. F. Gu†
Lawrence Livermore National Laboratory, Livermore, California 94550, USA
(Received 10 November 2009; published 25 January 2010)

The electric quadrupole ($E2$) and magnetic octupole ($M3$) ground-state transitions in Ni-like W^{46+} have been measured using high-resolution crystal spectroscopy at the LLNL electron-beam ion trap facility. The lines fall in the soft x-ray region near 7.93 Å and were originally observed as an unresolved feature in tokamak plasmas. Using flat ammonium dihydrogen phosphate and quartz crystals, the wavelengths, intensities, and polarizations of the two lines have been measured for various electron-beam energies and compared to intensity and polarization calculations performed using the Flexible Atomic Code (FAC).

DOI: 10.1103/PhysRevA.81.012505 PACS number(s): 32.30.Rj, 32.70.Fw

I. INTRODUCTION

The lowest excited levels of nickellike high-Z systems are the $(3s^2 3p^6 3d^4_{3/2} 3d^5_{5/2} 4s_{1/2})_{J=3,2}$ levels. These decay to the $(3s^2 3p^6 3d^{10})_{J=0}$ ground state via a magnetic octupole ($M3$) and an electric quadrupole ($E2$) transition, respectively. The populations of metastable levels, from which electric-dipole forbidden transitions originate, are density sensitive and therefore these transitions typically do not occur in dense plasmas. However, in the spectra from low-density sources such as tokamaks and electron-beam ion traps (EBITs), electric-dipole forbidden transitions can in fact be among the strongest lines, especially from high-Z ions where their transition probabilities are higher.

Magnetic octupole transitions were first observed by Beiersdorfer *et al.* in 1991 in nickellike thorium and uranium ions [1] at the LLNL electron-beam ion trap facility, and they were later studied by Träbert *et al.* [2–4] in nickellike xenon and neighboring ions. Electric quadrupole lines have been observed in many low-density laboratory plasmas; see, e.g., Refs. [5–7].

An unresolved Ni-like W^{46+} ion feature was previously observed at 7.93 Å in the ASDEX Upgrade tokamak by Neu *et al.* [8–10] and was interpreted as the $E2$ line. Based on calculations, Loch *et al.* [11] and Ralchenko *et al.* [12,13] have suggested that this feature was actually a blend of the $M3$ and $E2$ lines. Ralchenko calculated the line positions, line intensities, and density dependences of the lines [13]. Ralchenko *et al.* also observed the unresolved line in the NIST EBIT using a 4-pixel x-ray calorimeter spectrometer [12]. The feature has also been observed in the LLNL SuperEBIT using a 36-pixel x-ray calorimeter array [14].

Several authors have calculated the two line positions, for example, Aggarwal *et al.* [15], Fournier [16], Safronova *et al.* [17], Zhang *et al.* [18], and Ballance *et al.* [19]. Other calculations are limited to the $E2$ transition [20–23].

In the present study, the x-ray feature at 7.93 Å has been resolved and shown to consist of the two electric-dipole forbidden transitions. The lines were studied using high-resolution spectroscopy at the LLNL EBIT facility, and the measurement yields wavelengths with an uncertainty of about 0.6 mÅ.

The intensities of the two lines have been studied at several electron-beam energies, and the excitation energy dependence on the relative intensities in the $3.3 - 5.4$ keV beam-energy interval has been investigated using two flat-crystal spectrometers. The measured line ratios at nearly constant electron density show that the energy has little effect on the relative intensities. However, calculations performed using the Flexible Atomic Code (FAC) show that the density dependence is very strong for plasmas of interest in magnetic fusion research.

The emitted radiation from an EBIT is in general both anisotropic and polarized. By using two crystal spectrometers the relative polarizations of the two lines could be studied as a function of electron-excitation energy and compared to the predicted polarizations calculated with FAC. It is shown that both lines have very little polarization.

II. EXPERIMENTAL SETUP

The measurements were performed using the SuperEBIT electron-beam ion trap at the Lawrence Livermore National Laboratory [24,25]. In an EBIT, the atomic element of interest is injected into an electron beam with a density around 10^{11-12} cm^{-3}, where the atoms are ionized and excited by unidirectional electron collisions. The freshly produced ions are then trapped in a small region of the electron beam by a combination of electrostatic potentials and strong magnetic fields. The atomic charge state distribution of the trapped ions is determined by the electron-beam energy, ionization and recombination cross sections, charge exchange, and various trap parameters, such as drift tube voltages and trap cycle length. In the trap, the ions have little kinetic energy and no overall direction of motion; hence the Doppler effect does not limit the spectroscopic resolution or cause any line shift. The electron beam determines the volume in which the ions are produced, excited, and confined. This narrow spatial region defines the extent of the light source which can be spectroscopically imaged without the need for a spectrometer entrance slit.

SuperEBIT was operated in its low-energy mode, which is similar to the EBIT-I device [26], at six beam energies from 3.3 keV up to 8.6 keV, to provide data for different electron collision energies (Cu-like W^{45+} has an ionization potential

*Also at Department of Physics, Lund University, SE-221 00 Lund, Sweden.; clementson@llnl.gov.
†Present address: Space Sciences Laboratory, University of California, Berkeley, California 94720, USA.

of 2414.1 eV, while Ni-like W^{46+} ionizes at 4057 eV [27]). From a vial containing the crystalline compound tungsten hexacarbonyl, $W(CO)_6$, the sublimated material was injected into SuperEBIT as a gas through one of the ports surrounding the trap. Using two of the other drift tube ports, trimethylaluminum (TMA), $Al_2(CH_3)_6$, using a ballistic gas injector, and sodium gas, using a sublimation injector, were introduced into the trap in order to provide reference wavelength lines.

The soft x rays were measured using two flat-crystal spectrometers. A crystal diffracts radiation according to the Bragg law

$$n\lambda = 2d \sin\theta,$$

where n is the diffraction order, λ the wavelength, d the crystal lattice spacing, and θ the Bragg angle, i.e., the angle of incidence measured from the crystal surface. From Bragg's law the crystal resolving power R can be determined as

$$R = \frac{\lambda}{\Delta\lambda} = \frac{1}{\Delta\theta}\tan\theta.$$

Here $\Delta\theta$ is the the angular resolution of the spectrometer, which is limited by a combination of the source width, crystal structure, and detector resolution. For a given crystal and detector, large resolving powers can therefore be achieved either at large Bragg angles or at great distances between the source and crystal.

The first crystal spectrometer used here was a broadband instrument designed by Brown *et al.* [28]. The instrument employs long, flat crystals in a vacuum environment. For this measurement, an ammonium dihydrogen phosphate (ADP) (101) crystal with a $2d$ spacing of 10.640 Å [29] was positioned at a nominal Bragg angle of 48°. An ORDELA 1100 XF position-sensitive proportional counter fed data to a CAMAC data acquisition system that was controlled by KMAX software [30]. The ADP crystal, at a distance of 38 cm from the electron beam, diffracted the radiation to the proportional counter located 25.4 cm from the crystal rotation axis. The optical plane was perpendicular to the electron beam. The resolving power R was about 1450. A spectrum obtained at an electron-beam energy of 5340 eV shows the two tungsten lines together with the aluminum calibration lines, see Fig. 1.

The second spectrometer was a very-high-resolution flat-crystal instrument [31] equipped with a quartz $(10\bar{1}0)$ crystal,

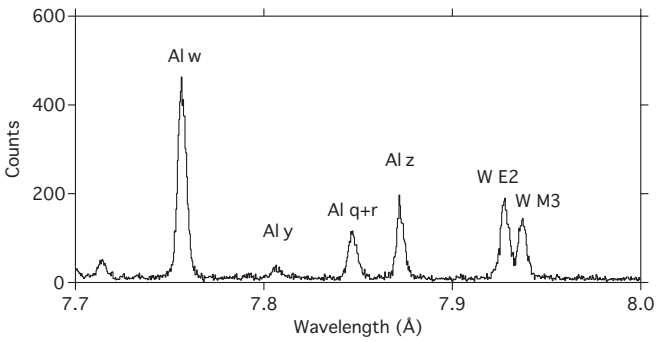

FIG. 1. Spectrum from the broadband spectrometer at a beam energy of 5340 eV showing the $M3$ and $E2$ lines of Ni-like W^{46+} together with the K-shell lines of heliumlike and lithiumlike aluminum.

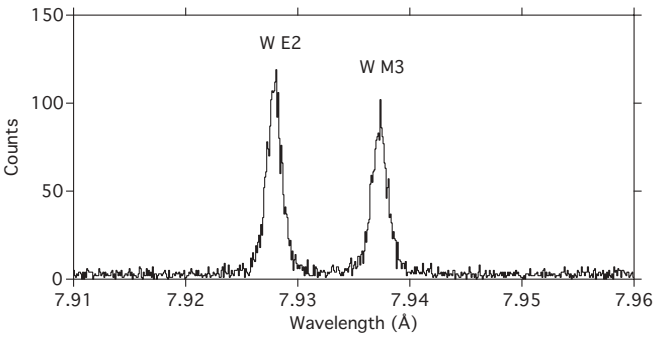

FIG. 2. Spectrum from the high-resolution spectrometer at a beam energy of 5350 eV showing the $M3$ and $E2$ lines of Ni-like W^{46+}.

and employing the same ORDELA detector. The crystal has a $2d$ spacing of 8.350 Å [32] and was positioned about 93 cm from the trap. The detector again was 25 cm from the crystal, which was set up at a Bragg angle of 72°. The spectrometer achieved a resolving power R of almost 5000. This is more than sufficient to fully resolve the two electric-dipole forbidden tungsten lines, as shown in Fig. 2.

Conversion factors used are $hc = 12398.42$ Å eV $=$ 8065.5410 eV cm, and 1 Ry $= 13.60569$ eV.

III. ANALYSIS

A. Wavelengths

The broadband spectrometer was used to determine the line positions for the $M3$ and $E2$ lines. The spectra acquired at the Bragg angle of 48° were wavelength calibrated using theoretical K-shell lines of He-like Al^{11+} (w $1s^2\,{}^1S_0$–$1s2p\,{}^1P_1$ at 7.75730 Å and z $1s^2\,{}^1S_0$–$1s2s\,{}^3S_1$ at 7.87212 Å) by Drake [33] and the Ly-γ lines of H-like Na^{10+} (8.02107 Å weighted average) by Garcia and Mack [34], cf. Fig. 1. Based on wavelength measurements of He-like O^{6+} [35] and He-like Ar^{16+} [36], the He-like Al^{11+} reference lines are believed to be accurate to 0.5 mÅ. The Bragg angle versus channel position dispersion was derived from a calibration spectrum and applied to a spectrum containing the tungsten lines together with the K-shell aluminum lines. There were small shifts of the observed Al z and Al w lines in this spectrum from the theoretical wavelengths, and the dispersion was adjusted to account for the observed average shift of the two reference lines. The uncertainties in anchoring the wavelength scale to the aluminum reference lines are estimated to be the maximum wavelength difference of the aluminum lines inferred from the calibration relative to the reference wavelengths, as well as the statistical uncertainties in the line positions of Al z and Al w. The wavelength dispersion uncertainty was evaluated for each line as a function of the distance from Al z. These uncertainties were added in quadrature with the counting statistics to give error bars of the measured line positions. The uncertainty in the splitting of the two tungsten lines is dominated by counting statistics, which, when added with the dispersion uncertainty, results in an error bar of 0.2 mÅ. In addition to the tungsten lines, the wavelength of the unresolved Li-like Al^{10+} lines q ($1s^22s^2S_{1/2}$–$1s2s2p^2P_{3/2}$) and r ($1s^22s^2S_{1/2}$–$1s2s2p^2P_{1/2}$)

TABLE I. Comparison of measured and calculated line positions of the tungsten $M3$ and $E2$ lines. Wave numbers and energies, where reported (from levels and transitions), have been converted to wavelengths.

Ni-like W^{46+}			
$M3$		$E2$	
Experiment (Å)	Theory (Å)	Experiment (Å)	Theory (Å)
7.9374(7)	7.9368[a]	7.9280(6)	7.9270[a]
	7.94883[b]		7.93921[b]
	7.9449[c]		7.9354[c]
	7.940[d]		7.930[d]
	7.938[e]		7.929[e]
	7.9477[f]		7.9380[f]
	7.94611[g]		7.93683[g]
			7.94205[h]
			7.91478[i]
			7.930[j]
			7.944[k]

Li-like Al^{10+}	Experiment (Å)	Theory (Å)
q	7.8473(6)	7.8460[l]
r		7.8479[l]

[a]This work (FAC).
[b]Aggarwal *et al.* (GRASP) [15].
[c]Fournier (RELAC) [16].
[d]Ralchenko *et al.* (FAC) [12].
[e]Safronova *et al.* (RMBPT) [17].
[f]Zhang *et al.* (DFS) [18].
[g]Ballance *et al.* (*R*-matrix) [19].
[h]Dong *et al.* (GRASP) [20].
[i]Safronova (Cowan) *et al.* [17].
[j]Safronova *et al.* (FAC) [21].
[k]Pütterich *et al.* (GRASP) [23].
[l]Vainshtein and Safronova ($1/Z$ expansion) [37].

was determined. The measured wavelengths of the lines are listed in Table I together with theoretical predictions.

B. Intensities

Line intensities were studied as a function of electron impact excitation energy using the broadband and high-resolution spectrometers. Both instruments measured at electron-beam energies from 3.3 to 5.4 keV. In addition, the broadband spectrometer measured at a beam energy of 8.6 keV. The observed relative intensities of the two lines are shown in Fig. 3.

C. Polarization

The emitted radiation can be divided into two polarization components, one with the electric-field vector in the z direction parallel to the electron beam, and one with the electric field in the plane perpendicular to the beam axis, that is,

$$I = I_{\parallel} + I_{\perp}.$$

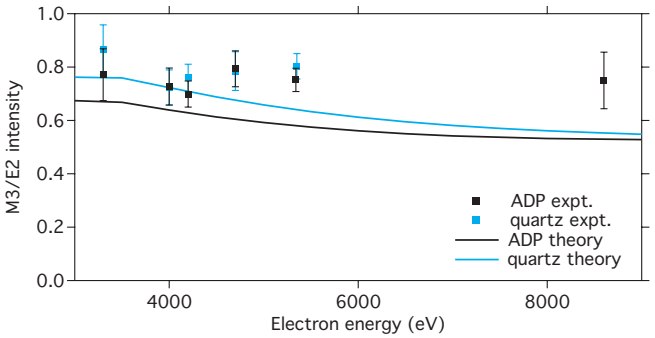

FIG. 3. (Color online) Intensity of the $M3$ vs the $E2$ line. Observed and calculated intensity ratios as a function of electron-beam energy.

Diffracting crystals have different reflectivities in the direction parallel to the beam, $R_{\parallel}$, and the direction within the dispersion plane, $R_{\perp}$. The observed intensity can then be expressed as

$$I_{\rm obs} = R_{\parallel} I_{\parallel} + R_{\perp} I_{\perp}.$$

The relative reflectivity $R = R_{\perp}/R_{\parallel}$ for ADP crystals has been calculated by Henke *et al.* [29] to be $R_{\rm ADP} = 0.06$. This reflectivity is very small, because the Bragg angle is close to 45°, where only parallel polarized light gets reflected. The reflectivities are functions of photon energy or, equivalently, of Bragg angle and can in general be modeled as $R = |\cos^m(2\theta)|$, where $1 \leqslant m \leqslant 2$ depending on whether the crystal can be considered perfect ($m = 1$) or mosaic ($m = 2$) [38]. As no published data exist on the quartz reflectivity, $R_{\rm quartz}$ is taken to be the geometric mean of the extreme cases with $m = 1$ and $m = 2$. The quartz relative reflectivity at 72° is thus taken to be $R_{\rm quartz} = 0.73$. Using this method for the ADP crystal gives a reflectivity of 0.03, which is quite close to the value by Henke *et al.* This indicates that the geometrical mean of the perfect and mosaic models makes a good estimate, which, as we show below, does not contribute a significant error to the analysis. The two tungsten lines are closely spaced, so the reflectivities are practically the same.

The measurements were carried out at an observation angle perpendicular to the electron beam. The polarization P at this angle can be expressed as

$$P = \frac{I_{\parallel} - I_{\perp}}{I_{\parallel} + I_{\perp}},$$

i.e., as the relative difference of the intensity of the radiation with electric field in the beam parallel direction and the beam perpendicular direction. The relative polarization of two lines can be measured when observed with two spectrometers. Using

$$P_{M3} = \frac{\left.\frac{I^{M3}}{I^{E2}}\right|_{\rm ADP}\left(1 + R_{\rm ADP}\frac{1-P_{E2}}{1+P_{E2}}\right)(R_{\rm quartz}+1) - \left.\frac{I^{M3}}{I^{E2}}\right|_{\rm quartz}\left(1 + R_{\rm quartz}\frac{1-P_{E2}}{1+P_{E2}}\right)(R_{\rm ADP}+1)}{\left.\frac{I^{M3}}{I^{E2}}\right|_{\rm ADP}\left(1 + R_{\rm ADP}\frac{1-P_{E2}}{1+P_{E2}}\right)(R_{\rm quartz}-1) - \left.\frac{I^{M3}}{I^{E2}}\right|_{\rm quartz}\left(1 + R_{\rm quartz}\frac{1-P_{E2}}{1+P_{E2}}\right)(R_{\rm ADP}-1)}$$

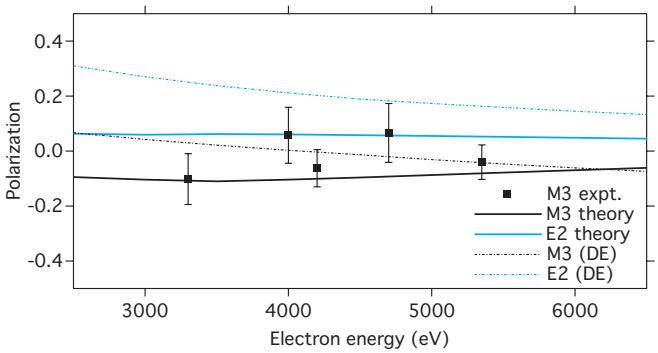

FIG. 4. (Color online) Theoretical and measured polarization of lines $M3$ and $E2$. The experimental data for the $M3$ line are tied to the theoretical polarization of the $E2$ line. Also shown are the calculated polarizations with direct excitation (DE) only.

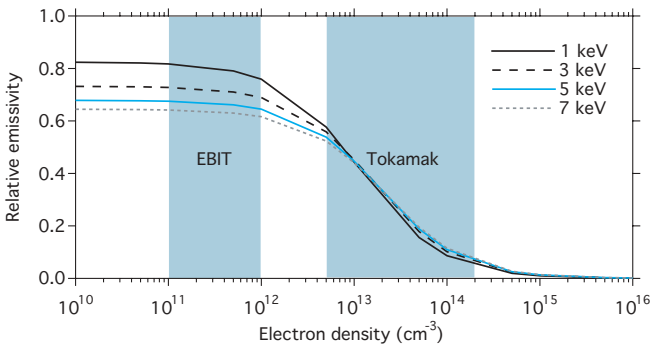

FIG. 5. (Color online) Calculated emissivity ratio of the $M3$ and $E2$ lines in a Maxwellian plasma for the temperatures listed. Typical EBIT and tokamak core densities are indicated by the shaded regions.

as shown in Ref. [39], the polarization of the $M3$ line can be expressed in terms of the polarization of the $E2$ line. The polarization of line $E2$ is taken to be a constant 5% in the interval observed, as the calculations indicate (see below). The appropriateness of choosing the geometric mean of the two limiting models for the quartz crystal reflectivity was assessed by studying the effects of this choice on the inferred polarization of the $M3$ line. Modeling the reflectivities as either perfect or mosaic resulted in changes of less than 0.02 for the inferred polarization. The largest contributions to the polarization uncertainties are from the statistics of the line intensities, giving error bars of up to 0.08. The uncertainties from the crystal reflectivities and the observed line intensities have been added in quadrature to estimate the polarization uncertainty. The inferred $M3$ polarization versus beam energy is shown together with the theoretical predictions in Fig. 4.

IV. THEORY

The spectrum of Ni-like W^{46+} was calculated using the Flexible Atomic Code, FAC v.1.1.1. FAC is a fully relativistic program for atomic-structure calculations and spectral modeling [40]. The nickellike system was modeled using configuration state functions consisting of $3s^2 3p^6 3d^{10}$, $3s^2 3p^6 3d^9 nl$, $3s^2 3p^5 3d^{10} nl$, and $3s 3p^6 3d^{10} nl$ with $n = 4$ and 5 and $l = 0, 1, \ldots, n-1$. The K and L shells were held closed in the structure calculation. To model the observed emission of the two electric-dipole forbidden lines, the intensities needed to be corrected for the crystal reflectivities, the line polarizations, and the anisotropic emission distributions from the EBIT plasma. These effects are taken into account by using the correction factor

$$G(E) = \left[1 + \frac{1-R}{1+R} P(E)\right] A(E),$$

where $P(E)$ and $A(E)$ are the calculated line polarization and anisotropy, respectively. The calculated intensities of the $M3$ versus $E2$ line at the EBIT experimental conditions are shown in Fig. 3 together with observed line ratios. The theoretical polarization is shown as a function of electron excitation energy in Fig. 4. To assess the effects of cascades on the line polarizations, a five-level model of the nickellike ion was studied with direct excitation (DE) as the only population mechanism.

Excluding polarization, the structure calculation was extended to $n = 6$, and the $M3$ and $E2$ line emissivities were studied as a function of electron density, see Fig. 5. These additional calculations were done for temperatures around 4 keV, which is the temperature when the nickellike tungsten abundance is expected to peak [23].

V. SUMMARY

The nickellike tungsten feature at 7.93 Å previously observed at the ASDEX Upgrade tokamak [8–10], the NIST EBIT [12], and the LLNL SuperEBIT [14] has now been fully resolved and shown to consist of two components: the electric-dipole forbidden ground-state transitions $M3$ at 7.9374(7) Å and $E2$ at 7.9280(6) Å. The theoretical wavelengths from our FAC calculations agree very well with the measured positions. The only other calculation that has such good agreement is the relativistic many-body perturbation theory (RMBPT) by Safronova *et al.* [17]. However, we note that the measured separation of 9.3(2) mÅ agrees better with other calculations [15,16,18]. An especially good match is achieved by the R-matrix calculation by Ballance *et al.* [19], who predicted a separation of 9.28 mÅ.

The $M3$ and $E2$ lines originate from the two lowest excited levels $(3d_{5/2}4s_{1/2})_{J=3,2}$. The calculations show that direct excitation is not the main population mechanism of the levels, but rather cascades, cf. Fig. 4. This causes the $E2$ line to have very little polarization. The calculations, which include cascades from levels as high as $n = 5$, show that the $E2$ line has a nearly constant linear polarization of only 5% over a large energy interval, which is significantly less than what results from direct excitation alone. The cascade population of the $J = 3$ level has the opposite effect, resulting in an increase in the magnitude of the polarization than what electron-impact excitation alone would cause. The measured polarization of the $M3$ line hovers around zero, appearing a bit smaller in magnitude than the predicted values, which range between -5 and -10%. Nickellike tungsten ionizes to cobaltlike tungsten at energies of 4057 eV and above, and then recombination can populate the two metastable levels in addition to the direct excitation and cascade population mechanisms. Recombination, however, is not included in

our model. Nevertheless, both the measured polarization and relative intensity values agree rather well with the calculations.

Electric-dipole forbidden lines are frequently used as plasma diagnostics, especially as a diagnostic for the electron density [41–43]. As indicated by our calculations, the two tungsten transitions can be used as a density diagnostic in plasmas of densities in the $10^{12} - 10^{15}$ cm^{-3} range. This interval coincides very well with plasmas of interest in magnetic fusion research, as illustrated in Fig. 5. For such plasmas, the temperature dependence on the relative line intensities is very weak, whereas the density dependence is strong, allowing one to make a rather robust measurement of the electron density.

The thermal line broadening in a tokamak plasma is smaller than the wavelength separation of the line pair. Doppler widths range from 1.5 mÅ at an ion temperature of 1 keV up to 4.0 mÅ at 8 keV. Spectrometers with resolving powers of 10 000 or higher may therefore be used to determine the ion temperature from the two lines in this range.

High-resolution observations of the Ni-like W^{46+} line pair could be a valuable diagnostic of magnetically confined plasmas, especially for those plasmas in which tungsten occurs as an indigenous trace element. The ITER tokamak, currently under construction, will have core temperatures in the 3–5 keV range during the initial ohmic phase. This is the interval in which W^{46+} ions are abundant in the core [23,44,45]. Diagnostics observing the $M3$ and $E2$ lines may thus play an important role in the ITER program.

ACKNOWLEDGMENTS

This work was performed under the auspices of the US Department of Energy by Lawrence Livermore National Laboratory under Contract DE-AC52-07NA-27344 and supported by LLNL Laboratory Directed Research and Development Contract 09-ERD-016. The authors would like to acknowledge support for the experiment from Dr. Greg Brown, Dr. Hui Chen, Phil D'Antonio, Miriam Frankel, Ed Magee, and Prof. Elmar Träbert. Albert Wynn from FAMU is acknowledged for assistance with the calculations. Joel Clementson would like to thank Dr. Hans Lundberg, Dr. Sven Huldt, and Prof. Sune Svanberg for their support.

[1] P. Beiersdorfer, A. L. Osterheld, J. Scofield, B. Wargelin, and R. E. Marrs, Phys. Rev. Lett. **67**, 2272 (1991).
[2] E. Träbert, P. Beiersdorfer, G. V. Brown, S. Terracol, and U. I. Safronova, Nucl. Instrum. Methods Phys. Res. B **235**, 23 (2005).
[3] E. Träbert, P. Beiersdorfer, G. V. Brown, K. Boyce, R. L. Kelley, C. A. Kilbourne, F. S. Porter, and A. Szymkowiak, Phys. Rev. A **73**, 022508 (2006).
[4] E. Träbert, P. Beiersdorfer, and G. V. Brown, Phys. Rev. Lett. **98**, 263001 (2007).
[5] M. Klapisch, J. L. Schwob, M. Finkenthal, B. S. Fraenkel, S. Egert, A. Bar-Shalom, C. Breton, C. DeMichelis, and M. Mattioli, Phys. Rev. Lett. **41**, 403 (1978).
[6] P. Beiersdorfer *et al.*, Phys. Rev. A **37**, 4153 (1988).
[7] N. K. Del Grande, P. Beiersdorfer, J. R. Henderson, A. L. Osterheld, J. H. Scofield, and J. K. Swenson, Nucl. Instrum. Methods Phys. Res. B **56-57**, 227 (1991).
[8] R. Neu, K. B. Fournier, D. Schlögl, and J. Rice, J. Phys. B **30**, 5057 (1997).
[9] R. Neu, K. B. Fournier, D. Bolshukhin, and R. Dux, Phys. Scr. **T92**, 307 (2001).
[10] R. Neu *et al.*, Plasma Phys. Control. Fusion **44**, 811 (2002).
[11] S. D. Loch, M. S. Pindzola, C. P. Ballance, D. C. Griffin, A. D. Whiteford, and T. Pütterich AIP Conf. Proc. **874**, 233 (2006).
[12] Yuri Ralchenko, Joseph N. Tan, J. D. Gillasy, Joshua M. Pomeroy, and Eric Silver, Phys. Rev. A **74**, 042514 (2006).
[13] Y. Ralchenko, J. Phys. B **40**, F175 (2007).
[14] J. Clementson, P. Beiersdorfer, G. V. Brown, and M. F. Gu, Phys. Scr. **81**, 015301 (2010).
[15] K. M. Aggarwal, P. H. Norrington, K. L. Bell, F. P. Keenan, G. J. Pert, and S. J. Rose, At. Data Nucl. Data Tables **74**, 157 (2000).
[16] K. B. Fournier, At. Data Nucl. Data Tables **68**, 1 (1998).
[17] U. I. Safronova, A. S. Safronova, S. M. Hamasha, and P. Beiersdorfer, At. Data Nucl. Data Tables **92**, 47 (2006).
[18] H. L. Zhang, D. H. Sampson, and C. J. Fontes, At. Data Nucl. Data Tables **48**, 91 (1991).
[19] C. P. Ballance and D. C. Griffin, J. Phys. B **39**, 3617 (2006).
[20] C. Z. Dong, S. Fritzsche, and L. Y. Xie, J. Quant. Spectrosc. Radiat. Transf. **76**, 447 (2003).
[21] A. S. Safronova *et al.*, Can. J. Phys. **86**, 267 (2008).
[22] S. M. Hamasha, A. S. Shlyaptseva, and U. I. Safronova, Can. J. Phys. **82**, 331 (2004).
[23] T. Pütterich, R. Neu, R. Dux, A. D. Whiteford, and M. G. O'Mullane, (ASDEX Upgrade Team), Plasma Phys. Control. Fusion **50**, 085016 (2008).
[24] P. Beiersdorfer, Can. J. Phys. **86**, 1 (2008).
[25] R. E. Marrs, Can. J. Phys. **86**, 11 (2008).
[26] M. A. Levine, R. E. Marrs, J. R. Henderson, and M. B. Knapp, and D. A. Schneider, Phys. Scr. **T22**, 157 (1988).
[27] A. E. Kramida and J. Reader, At. Data Nucl. Data Tables **92**, 457 (2006).
[28] G. V. Brown, P. Beiersdorfer, and K. Widmann, Rev. Sci. Instrum. **70**, 280 (1999).
[29] B. L. Henke, E. M. Gullikson, and J. C. Davis, At. Data Nucl. Data Tables **54**, 181 (1993).
[30] P. Beiersdorfer, G. V. Brown, L. Hildebrandt, and K. L. Wong, Rev. Sci. Instrum. **72**, 508 (2001).
[31] P. Beiersdorfer, J. R. Crespo López-Urrutia, E. Förster, J. Mahiri, and K. Widmann, Rev. Sci. Instrum. **68**, 1077 (1997).
[32] A. Burek, Space Sci. Instrum. **2**, 53 (1976).
[33] G. W. Drake, Can. J. Phys. **66**, 586 (1988).
[34] J. D. Garcia and J. E. Mack, J. Opt. Soc. Am. **55**, 654 (1965).
[35] L. Engström and U. Litzén, J. Phys. B **28**, 2565 (1995).
[36] R. D. Deslattes, H. F. Beyer, and F. Folkmann, J. Phys. B **17**, L689 (1984).
[37] L. A. Vainshtein and U. I. Safronova, At. Data Nucl. Data Tables **21**, 49 (1978).
[38] P. Beiersdorfer, J. R. Crespo López-Urrutia, V. Decaux, K. Widmann, and P. Neill, Rev. Sci. Instrum. **68**, 1073 (1997).

[39] P. Beiersdorfer, G. Brown, S. Utter, P. Neill, K. J. Reed, A. J. Smith, and R. S. Thoe, Phys. Rev. A **60**, 4156 (1999).
[40] M. F. Gu, Can. J. Phys. **86**, 675 (2008).
[41] R. W. P. McWhirter, Phys. Rep. **37**, 165 (1978).
[42] F. Bely-Dubau, Phys. Scr. **T7**, 34 (1984).
[43] H. R. Griem, *Principles of Plasma Spectroscopy* (Cambridge University Press, New York, 1997).
[44] C. H. Skinner, Can. J. Phys. **86**, 285 (2008).
[45] N. J. Peacock, M. G. O'Mullane, R. Barnsley, and M. Tarbutt, Can. J. Phys. **86**, 277 (2008).